

Giant magnon spin conductivity approaching the two-dimensional transport regime in ultrathin yttrium iron garnet films

X-Y. Wei^{1,*}, O. Alves Santos¹, C.H. Sumba Lusero^{1,†}, G. E. W. Bauer^{1,2}, J. Ben Youssef³, and B. J. van Wees¹

¹Physics of Nanodevices, Zernike Institute for Advanced Materials, University of Groningen, Nijenborgh 4, 9747 AG Groningen, The Netherlands

²WPI-AIMR & Institute for Materials Research & CSRN, Tohoku University, Sendai 980-8577, Japan

³Lab-STICC, CNRS- UMR 6285, Université de Bretagne Occidentale, 6 Avenue Le Gorgeu, 29238 Brest Cedex 3, France

*e-mail: x.wei@rug.nl

[†]Current address: Leibniz Institute for Solid State and Materials Research, IFW, 01069 Dresden, Germany

Conductivities are key material parameters that govern various types of transport (electronic charge, spin, heat etc.) driven by thermodynamic forces. Magnons, the elementary excitations of the magnetic order, flow under the gradient of a magnon chemical potential¹⁻³ in proportion to a magnon (spin) conductivity σ_m . The magnetic insulator yttrium iron garnet (YIG) is the material of choice for efficient magnon spin transport. Here we report an unexpected giant σ_m in record-thin YIG films with thicknesses down to 3.7 nm when the number

of occupied two-dimensional (2D) subbands is reduced from a large number to a few, which corresponds to a transition from 3D to 2D magnon transport. We extract a 2D spin conductivity (≈ 1 S) at room temperature, comparable to the (electronic) spin conductivity of the high-mobility two-dimensional electron gas in GaAs quantum wells at millikelvin temperatures⁴. Such high conductivities offer unique opportunities to develop low-dissipation magnon-based spintronic devices.

The spin current density in metals is the difference of the up- and down-spin charge current densities measured in A/m^2 , which is driven by a gradient of the spin chemical potential (often called spin accumulation) $\nabla\mu_s$. The spin conductivity σ , defined as $j_s = j_\uparrow - j_\downarrow = \sigma_s \nabla\mu_s/e$, can be expressed in electrical units as S/m. In a magnetic insulator where charge currents are absent, each magnon carries angular momentum \hbar , which is equivalent to the spin current in metals carried by a pair of spin-up ($+\hbar/2$) and spin-down ($-\hbar/2$) electrons that flow in opposite directions. A magnon current j_m can be defined as its number current times electron charge e . In magnetic insulator-based spintronic devices, magnon spin currents are injected, detected, and modulated by microwave striplines or electric contacts made from a heavy metal for charge-spin conversion⁵⁻⁹. The corresponding spin conductivity, magnon conductivity σ_m , is the current density divided by the gradient of the magnon chemical potential. The unit of the magnon conductivity in $j_m = \sigma_m \nabla\mu_m/e$, where μ_m is the magnon chemical potential, is then the same as that of electrons in a metal¹. The value of $\sigma_m = 4 \times 10^5$ S/m in a 210 nm thick YIG film at room temperature⁶ corresponds to the electronic conductivity of bad metals.

The high magnetic and acoustic quality of magnetic insulators make them the ideal material for all-magnon logical circuits and magnon-based quantum information^{10,11}. An example of recent progress in magnon-based computing is an integrated magnonic half-adder based on 350 nm wide wave guides made from 85-nm-thick YIG films¹². However, these devices operate with coherent magnons (\sim GHz) excited by narrow microwave striplines which can not be integrated into an all-electrical circuit. Therefore, it is attractive to inject magnons electrically¹³, but those are mainly thermal (\sim THz) and scatter much stronger at phonons. Also, scalability to smaller structure sizes, essential for future high-performance processing units, requires micro and nanofabrication in all dimensions. The first step is the growth of films of a few or even a single unit cell. Previously, magnon transport was reported in transistor structures on films down to about 10 nm, which shows that ultrathin films can maintain high quality and display intriguing non-linear magnon effects^{14,15}. However, the scattering by surface roughness is expected to increase in even thinner films¹⁶. This could be an obstacle for magnon spin transport in ultrathin YIG films that hinders observation of a transition from three dimensional magnons to two dimensional magnon gas when the thermal wavelength $\lambda_{\text{thermal}} = 2\pi\sqrt{\hbar\gamma D/(k_B T)}$ (~ 3 nm at room temperature) approaches the thickness of the films t_{YIG} , where \hbar is the reduced Planck constant, γ is the gyromagnetic ratio, D is spin wave stiffness and k_B is Boltzmann constant.

Here we report measurements of the magnon conductivity of YIG films with thicknesses down to 3.7 nm. Much to our surprise, the magnon transport turns out to be strongly enhanced in the ultrathin regime. We report a drastical increase in magnon conductivity of up to $\sigma_m = 1.6 \times 10^8$ S/m at room temperature that even exceeds the electronic spin conductivity of high-

purity copper. This increase is intimately connected to the small number of occupied subbands and apparent domination by the lowest subband in our films. These results can importantly boost the performance of magnon-based information technology^{10,17}.

We employ a non-local configuration⁶ (Figure 1a) of two Pt thin film strips with length L at a distance d on top of YIG films grown on gallium gadolinium garnet (GGG) by liquid phase epitaxy. An electric charge current I through the injector generates a transverse spin current due to the spin Hall effect¹⁸, resulting in a spin accumulation μ_s in Pt at the interface to YIG. The injector-conversion coefficient $\eta_{\text{inj}} = \mu_s/(eI)$ depends on the properties and dimensions of the Pt strip as explained in the Section I of the supplementary information (SI Section I). The effective interface spin conductance results from the exchange interaction across the interface and produces a magnon chemical potential μ_m on the YIG side of the interface that acts as a *magnon source*, where $\mu_m \approx \mu_s$ since the interface spin resistance can be ignored (see SI Section III). The detector electrode is a *magnon drain* that absorbs magnons and converts them into a spin current j_s entering the Pt detector electrode. The inverse spin Hall effect generates a detector voltage V_{nl} with detector-conversion coefficient $\eta_{\text{det}} = V_{\text{nl}}/j_s^{\text{det}}$. By reciprocity, $\eta_{\text{inj}} = \eta_{\text{det}}$ when injector and detector contacts have the same properties (see SI Section I for details). Since the signal scales with L , a normalized non-local resistance can be defined as $R_{\text{nl}} = V_{\text{nl}}/(IL)$. The magnon conductance follows from the measured non-local resistance

$$G_m = \frac{1}{\eta_{\text{inj}}\eta_{\text{det}}} \frac{V_{\text{nl}}}{I} = \frac{R_{\text{nl}}L}{\eta_{\text{inj}}\eta_{\text{det}}}. \quad (1)$$

The magnon conductivity σ_m as a function of the thickness t_{YIG} of the YIG films in Figure 1 then

follows from the magnon spin conductance

$$\sigma_m = \frac{G_m d}{t_{\text{YIG}} L}. \quad (2)$$

For the films with t_{YIG} much smaller than the magnon relaxation length λ_m as well as the lateral device dimension, μ_m can be considered constant in the z direction. Therefore, we use following equation to describe magnon diffusion^{6,19}

$$R_{\text{nl}} = \frac{\sigma_m t_{\text{YIG}} \eta_{\text{inj}} \eta_{\text{det}}}{\lambda_m} \text{csch} \frac{d}{\lambda_m} \rightarrow \begin{cases} \frac{\sigma_m t_{\text{YIG}} \eta_{\text{inj}} \eta_{\text{det}}}{d} & d \ll \lambda_m \\ \frac{2\sigma_m t_{\text{YIG}} \eta_{\text{inj}} \eta_{\text{det}}}{\lambda_m} \exp(-\frac{d}{\lambda_m}) & d \gg \lambda_m \end{cases}. \quad (3)$$

When the spacing d is smaller than λ_m , it is the Ohmic regime in which the magnons are conserved, $R_{\text{nl}}(G_m) \sim d^{-1}$. Otherwise, the signal decays exponentially as a function of distance due to magnon relaxation.

We measure R_{nl} at room temperature as a function of an external in-plane magnetic field \mathbf{H}_{ex} with $|\mathbf{H}_{\text{ex}}| = 50$ mT, which we rotate in the plane (Figure 1a). We modulate the AC current I by a low frequency (18 Hz) and detect the first/second harmonic signal $V_{\text{nl}}(\omega)/V_{\text{nl}}(2\omega)$ by lock-in amplifiers (see Methods). $V_{\text{nl}}(2\omega)$ depends on the spin Seebeck generation and diffusion of magnons under an inhomogeneous temperature profile, which renders interpretation difficult^{20,21} (see SI Section V). Therefore, we focus on $V_{\text{nl}}(\omega)$ that follows the formula

$$R_{\text{nl}}^{1\omega}(\alpha) = R_{\text{nl}}^{1\omega} \cos^2 \alpha + R_0^{1\omega}, \quad (4)$$

where $R_0^{1\omega}$ is an offset resistance (see Methods) and α is the angle of \mathbf{H}_{ex} with the x -axis. In Figure. 2, the the angle-dependent measurements in various thickness YIG films show that $R_{\text{nl}}^{1\omega}$ becomes four times larger when the film is over fifty times thinner from 210 nm to 3.7 nm. We also

observe a strongly increased non-local signal in ultrathin films in Figure 3 as a function of contact separation for a wide range of t_{YIG} including results on ultrathin YIG films for 400 nm wide Pt strips and for thicker films $t_{\text{YIG}} \geq 210 \text{ nm}$ ^{6,22}. Figure 4a emphasizes the dramatic enhancement of $R_{\text{nl}}^{1\omega}$ for the thinnest films down to $t_{\text{YIG}} = 3.7 \text{ nm}$ and fixed $d = 2.5 \mu\text{m}$, which can be attributed to the t_{YIG} dependence of σ_m because $\lambda_m > 2.5 \mu\text{m}$ for all thicknesses (see SI Section IV for details). $R_{\text{nl}}^{1\omega}$ *increases* with *decreasing* thickness and saturates for both the thinnest and thickest films.

A finite-element model¹ can simulate the depth (z) dependence of μ_m when $t_{\text{YIG}} > \lambda_m$ (see SI Section I for details). This leads to a limiting $\sigma_m \rightarrow 3 \times 10^4 \text{ S/m}$ in Figure 4b for thicker films, which represents the bulk value. The simulated R_{nl} values for $d = 2.5 \mu\text{m}$ in Figure 4c have been fitted to $R_{\text{nl}}^{1\omega}$ in Figure 4a by conductivities that are strongly enhanced in the regime $t_{\text{YIG}} < \lambda_m$. For $t_{\text{YIG}} = 3.7 \text{ nm}$, the magnon conductivity $\sigma_m = 1.6 \times 10^8 \text{ S/m}$ is *four orders of magnitude larger* compared to the bulk value, exceeding the electronic conductivity of pure metals such as copper with $\sigma_e = 6 \times 10^7 \text{ S/m}$ ²³. The observed saturation at $t_{\text{YIG}} \rightarrow 0$ appears to reflect an increased role of surface roughness scattering that we do not model explicitly.

A magnon conductivity that diverges for $t_{\text{YIG}} \rightarrow 0$ like $\sigma_m \sim \sigma_m^{2\text{D}} t_{\text{YIG}}^{-1}$ simply suggests two-dimensional transport. In Figure 4c, it shows that $\sigma_m^{2\text{D}}$ saturates for $t_{\text{YIG}} < 10 \text{ nm}$, i.e. higher 2D subbands do not contribute significantly even though they are still populated (see below). Extrapolation to zero thickness leads to $\sigma_m^{2\text{D}} \approx 1 \text{ S}$. This value at room temperature is comparable to that of the high-mobility two-dimensional electron gas at millikelvin temperatures, which is $\sigma_e^{2\text{D}} \approx 1.4 \text{ S}$ in GaAs quantum wells⁴.

The magnons propagate in the plane with wave vector \mathbf{k} and form perpendicular standing spin waves (PSSW) in z direction labeled by an integer n . The exchange interaction scales like $\sim k^2$ and dominates the magnon dispersion ε_{nk} at thermal energies ($\approx k_B T$) with small magnetodipolar corrections. A magnon with energy $\varepsilon_{nk} = \hbar\gamma D (k^2 + (n\pi/t_{\text{YIG}})^2)$ contributes to the conduction proportional to its thermal occupation $N_{nk} = 1/\{\exp[\varepsilon_{nk}/(k_B T)] - 1\}$. For YIG $\gamma/2\pi = 28 \text{ GHz/T}$ and the spin wave stiffness²⁴ $D = 5 \times 10^{-17} \text{ Tm}^2$. The highest occupied subband n defined as

$$n = \text{int} \left(\frac{t_{\text{YIG}}}{\pi} \sqrt{\frac{k_B T}{\hbar\gamma D}} \right) \quad (5)$$

at $\varepsilon_{n0} < k_B T$ as a function of thickness²⁵, where $\text{int}(x)$ is the greatest integer no more than x . For $t_{\text{YIG}} = 3.7 \text{ nm}$, only three approximately 2D subbands are occupied at room temperature.

The simplest model for the magnon conductivity in ν ($=2, 3$) dimensions follows from the Boltzmann equation with a constant relaxation time τ

$$\sigma_m^{(\nu)} = \frac{e^2 \tau^{(\nu)}}{k_B T} \int \frac{d\mathbf{k}}{(2\pi)^\nu} \left(\frac{\partial \varepsilon_k}{\hbar \partial k_z} \right)^2 \frac{e^{\varepsilon_k/(k_B T)}}{(e^{\varepsilon_k/(k_B T)} - 1)^2} \quad (6)$$

where $\varepsilon_k = \hbar\gamma D k^2$. Magnetic freeze-out experiments show that the contributions from the low-frequency magnons ($\sim \text{GHz}$) is significant even at room temperature, presumably reflecting low mobilities of thermal exchange magnons^{26–28}. This can be represented by a high momentum cut-off $K_\infty \sim 1/\text{nm}$ at magnon frequencies $\varepsilon_\infty/\hbar \sim \text{THz}$. In the high temperature limit $k_B T \gg \varepsilon_k$ the conductivities do not depend on γD :

$$\sigma_m^{(3)} = \frac{2e^2 k_B T \tau^{(3)}}{3\hbar^2 \pi^2} K_\infty, \quad (7)$$

$$\sigma_m^{(2)} = \frac{e^2 k_B T \tau^{(2)}}{\pi \hbar^2} \log \frac{K_\infty}{K_0}, \quad (8)$$

where K_0 is a low momentum cutoff by the magnon gap of $\varepsilon_0/\hbar \sim \text{GHz}$. By equating these equations with the experimental results $\sigma_m^{(3)} \approx 3 \times 10^4 \text{ S/m}$ and the present $\sigma_m^{(2)} \approx 1 \text{ S}$ and using the scattering times as adjustable parameters, we arrive at $\tau^{(3)} \approx 40 \text{ fs}$ and $\tau^{(2)} \approx 0.1 \text{ ns}$. The short scattering time in three dimensions can be explained by highly efficient magnon-phonon scattering at room temperature¹. While the high-momentum cut-off plays an important role in 3 dimensions, the near independence of $\sigma_m^{(2)}$ emphasizes the importance of the near band-gap excitations for transport in two dimensions. Coherent magnons excited at GHz frequencies can propagate over cm's in spite of their small group velocity because they scatter only weakly at phonons²⁹. Their contribution has a much larger effect on transport in ultrathin films than in the bulk, which is consistent with the magnetic field and temperature dependence reported in the SI. The estimated scattering time of $\tau^{(2)} = 0.1 \text{ ns}$ may be limited by the film roughness scattering. The precise mechanism can be elucidated only by more extensive experimental and theoretical studies of the temperature and field dependence.

While magnon-based devices do not suffer from Joule heating, magnon transport is not dissipationless^{6,30} even for transport on length scales shorter than the magnon relaxation length where magnons are conserved. The observed giant magnon conductivity is therefore excellent news, implying low dissipation from magnon-phonon scattering even at room temperature. Ultrathin films can therefore be driven with relative ease into the non-linear regime in e.g. magnon spin transistors^{14,15}, facilitating electrically-induced magnon Bose-Einstein condensation and magnon spin superfluidity^{31–33}. The robustness of the transport of the magnetic order for thin films of close to the monolayer thickness should allow magnon transport in nanostructures such as constrictions,

wires and dots with feature sizes of a few nanometer without loss of magnetic functionality.

Methods

Fabrication The YIG films are grown on $\text{Gd}_3\text{Ga}_5\text{O}_{12}$ (GGG) substrates by liquid-phase epitaxy (LPE) at the Université de Bretagne Occidentale in Brest, France, with thicknesses from 3.7 nm to 53 nm. The effective magnetization M_{eff} ($H_k - 4\pi M_s$) and the magnetic relaxation (intrinsic damping parameter α and extrinsic inhomogeneous linewidth ΔH_{in}) are determined by broadband ferromagnetic resonance (FMR) in the frequency range 2-40 GHz (see SI Section IV). The device patterns are written by three e-beam lithography steps, each followed by a standard deposition and lift-off procedure. The first step produces a Ti/Au marker pattern, used to align the subsequent steps. The second step defines the platinum injector and detector strips, as deposited by dc sputtering in an Ar+ plasma at an argon pressure with thickness ~ 8 nm for all devices. The third step defines 5/75 nm Ti/Au leads and bonding pads, deposited by e-beam evaporation. Devices have an injector/detector length $L = 30/25 \mu\text{m}$ and the strip widths W are 400 nm for series A and 100 nm for series B. The experimental results in main text are obtained from series A. The distance-dependent non-local resistances for series B can be found in SI Section III.

Measurements All measurements were carried out by means of three SR830 lock-in amplifiers using excitation frequency of 18 Hz. The lock-in amplifiers are set up to measure the first and second harmonic responses of the sample. Current was sent to the sample using a custom built current source, galvanically isolated from the rest of the measurement equipment. Voltage measurements

were made using a custom-built pre-amplifier (gain 10^3) and amplified further using the lock-in systems. The typical excitation currents applied to the samples are $200\text{ }\mu\text{A}$ (RMS) for series A and $20\text{ }\mu\text{m}$ for series B. The in-plane coercive field of the YIG B_c is below 10 mT for all YIG samples, and we apply an external field to orient the magnetization using a physical property measurement system (PPMS). The samples are mounted on a rotatable sample holder with stepper motor. All experimental data in the main text have been collected at 300 K (room temperature) at an applied magnetic field of 50 mT.

Simulations Our finite-element model implements the magnon diffusion equation in insulators in order to simulate transport of electrically injected magnons. We carried out the simulations by COMSOL MULTIPHYSICS (version 5.4) software package with technical details in the SI Section I.

Acknowledgements

We acknowledge the helpful discussion with J. Shan and T. Yu. We acknowledge the technical support from J. G. Holstein, H. de Vries, H. Adema, T. Schouten and A. Joshua. This work is part of the research programme "Skyrmionics" with project number 170, which is financed by the Dutch Research Council (NWO). The support by NanoLab NL and the Spinoza Prize awarded in 2016 to B. J. van Wees by NWO is also gratefully acknowledged. G.B. was supported by JSPS Kakenhi Grant 19H00645.

Author contributions

B.J.v.W. and X.W. conceived the experiments. X.W. designed and carried out the experiments, with help from O.A.S. J.B.Y. supplied the YIG samples used in the fabrication of devices. X.W., O.A.S., C.H.S.L., G.E.W.B. and B.J.v.W. were involved in the analysis. X.W. wrote the paper with O.A.S., G.E.W.B. and B.J.v.W. All authors commented on the manuscript.

References

1. Cornelissen, L. J., Peters, K. J. H., Bauer, G. E. W., Duine, R. A. & van Wees, B. J. Magnon spin transport driven by the magnon chemical potential in a magnetic insulator. *Phys. Rev. B* **94**, 014412 (2016).
2. Chunhui, D. *et al.* Control and local measurement of the spin chemical potential in a magnetic insulator. *Science* **357**, 195–198 (2017).
3. Olsson, K. S. *et al.* Pure spin current and magnon chemical potential in a nonequilibrium magnetic insulator. *Phys. Rev. X* **10**, 021029 (2020).
4. Chung, Y. J. *et al.* Ultra-high-quality two-dimensional electron systems. *Nature Materials* **20**, 632–637 (2021).
5. Brataas, A., van Wees, B., Klein, O., de Loubens, G. & Viret, M. Spin insulatronics. *Physics Reports* **885**, 1–27 (2020).

6. Cornelissen, L. J., Liu, J., Duine, R. A., Ben Youssef, J. & van Wees, B. J. Long-distance transport of magnon spin information in a magnetic insulator at room temperature. *Nature Physics* **11**, 1022–1026 (2015).
7. Lebrun, R. *et al.* Tunable long-distance spin transport in a crystalline antiferromagnetic iron oxide. *Nature* **561**, 222–225 (2018).
8. Chumak, A. V., Serga, A. A. & Hillebrands, B. Magnon transistor for all-magnon data processing. *Nature Communications* **5**, 4700 (2014).
9. Cornelissen, L. J., Liu, J., van Wees, B. J. & Duine, R. A. Spin-current-controlled modulation of the magnon spin conductance in a three-terminal magnon transistor. *Phys. Rev. Lett.* **120**, 097702 (2018).
10. Barman, A. *et al.* The 2021 Magnonics Roadmap. *Journal of Physics: Condensed Matter* **33**, 413001 (2021).
11. Chumak, A. *et al.* Roadmap on Spin-Wave Computing. Preprint at: <https://arxiv.org/abs/2111.00365> (2021).
12. Wang, Q. *et al.* A magnonic directional coupler for integrated magnonic half-adders. *Nature Electronics* **3**, 765–774 (2020).
13. Althammer, M. All-electrical magnon transport experiments in magnetically ordered insulators. *physica status solidi (RRL) –Rapid Research Letters* **15**, 2100130 (2021).

14. Wimmer, T. *et al.* Spin transport in a magnetic insulator with zero effective damping. *Phys. Rev. Lett.* **123**, 257201 (2019).
15. Liu, J., Wei, X.-Y., Bauer, G. E. W., Youssef, J. B. & van Wees, B. J. Electrically induced strong modulation of magnon transport in ultrathin magnetic insulator films. *Phys. Rev. B* **103**, 214425 (2021).
16. Yu, T., Sharma, S., Blanter, Y. M. & Bauer, G. E. W. Surface dynamics of rough magnetic films. *Phys. Rev. B* **99**, 174402 (2019).
17. Li, Y. *et al.* Hybrid magnonics: Physics, circuits, and applications for coherent information processing. *Journal of Applied Physics* **128**, 130902 (2020).
18. Sinova, J., Valenzuela, S. O., Wunderlich, J., Back, C. H. & Jungwirth, T. Spin Hall effects. *Rev. Mod. Phys.* **87**, 1213–1260 (2015).
19. Takahashi, S. & Maekawa, S. Spin injection and detection in magnetic nanostructures. *Phys. Rev. B* **67**, 052409 (2003).
20. Uchida, K. *et al.* Observation of the spin Seebeck effect. *Nature* **455**, 778–781 (2008).
21. Gomez-Perez, J. M., Vélez, S., Hueso, L. E. & Casanova, F. Differences in the magnon diffusion length for electrically and thermally driven magnon currents in $\text{Y}_3\text{Fe}_5\text{O}_{12}$. *Phys. Rev. B* **101**, 184420 (2020).
22. Shan, J. *et al.* Influence of yttrium iron garnet thickness and heater opacity on the nonlocal transport of electrically and thermally excited magnons. *Phys. Rev. B* **94**, 174437 (2016).

23. Laughton, M. A. & Say, M. G. *Electrical engineer's reference book* (Elsevier, 2013).
24. Klingler, S. *et al.* Measurements of the exchange stiffness of YIG films using broadband ferromagnetic resonance techniques. *Journal of Physics D: Applied Physics* **48**, 015001 (2014).
25. Stamps, R. & Camley, R. *Solid State Physics*. No. Volume 65 in Solid State Physics (Elsevier Science, 2014).
26. Kikkawa, T. *et al.* Critical suppression of spin Seebeck effect by magnetic fields. *Phys. Rev. B* **92**, 064413 (2015).
27. Jin, H., Boona, S. R., Yang, Z., Myers, R. C. & Heremans, J. P. Effect of the magnon dispersion on the longitudinal spin Seebeck effect in yttrium iron garnets. *Phys. Rev. B* **92**, 054436 (2015).
28. Jamison, J. S. *et al.* Long lifetime of thermally excited magnons in bulk yttrium iron garnet. *Phys. Rev. B* **100**, 134402 (2019).
29. Streib, S., Vidal-Silva, N., Shen, K. & Bauer, G. E. W. Magnon-phonon interactions in magnetic insulators. *Phys. Rev. B* **99**, 184442 (2019).
30. Man, H. *et al.* Direct observation of magnon-phonon coupling in yttrium iron garnet. *Phys. Rev. B* **96**, 100406 (2017).
31. Bender, S. A., Duine, R. A. & Tserkovnyak, Y. Electronic Pumping of Quasiequilibrium Bose-Einstein-Condensed Magnons. *Phys. Rev. Lett.* **108**, 246601 (2012).
32. Demokritov, S. O. *et al.* Bose-Einstein condensation of quasi-equilibrium magnons at room temperature under pumping. *Nature* **443**, 430–433 (2006).

33. Divinskiy, B. *et al.* Evidence for spin current driven Bose-Einstein condensation of magnons. *Nature Communications* **12**, 6541 (2021).

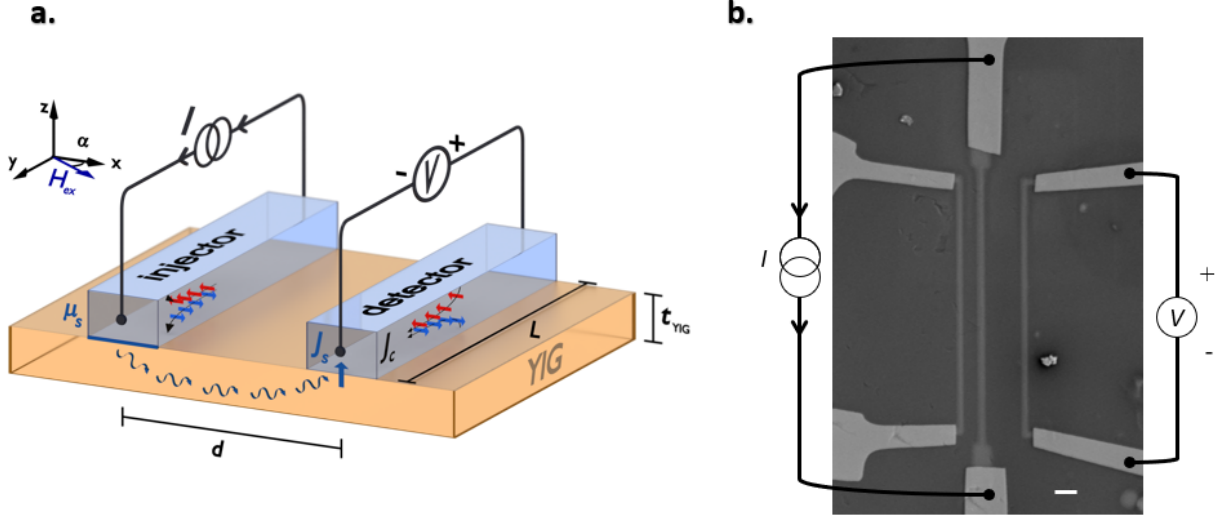


Figure 1: Device layout: **a)** Schematic representation of the experimental geometry. Two Pt strips deposited on top of YIG serve as magnon detector and injector via the direct and inverse spin hall effect. A low-frequency ac current with rms value of I_{ac} through the left Pt strip injects magnons. The center-to-center distance of the injector and the detector is d and the length of the injector/detector is L . A spin accumulation μ_s is formed at Pt|YIG interface due to the SHE when a charge current passes through the injector and excites magnon non-equilibrium underneath the injector. The diffusive magnons are absorbed at the drain, which induce a spin current density j_s . Using a lock-in technique, the first harmonic voltage is measured simultaneously by the right Pt strip, i.e. a magnon detector. α is the angle of external magnetic field H_{ex} . **b)** SEM image of the geometry. The parallel vertical lines are the platinum injector and detector, and they are contacted by gold leads. Current and voltage connections are indicated schematically. The scale bar represents $2 \mu\text{m}$.

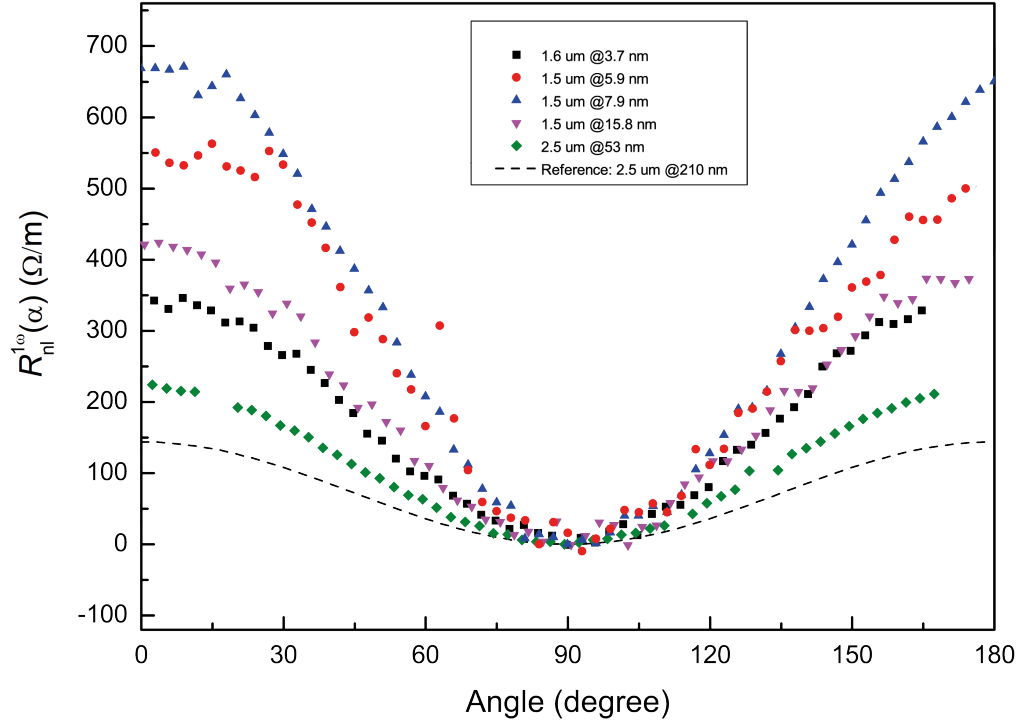


Figure 2: Dependence of non-local resistance on magnetization direction on ultrathin YIG films, for short center-to-center distances between the injector and the detector. The offset $R_0^{1\omega}$ in Eq.4 has been subtracted. This shows $R_{nl}^{1\omega}$ increases with decreasing thickness. Comparing with the reference from Cornelissen et al.⁶, $R_{nl}^{1\omega}$ significantly increases in ultrathin films.

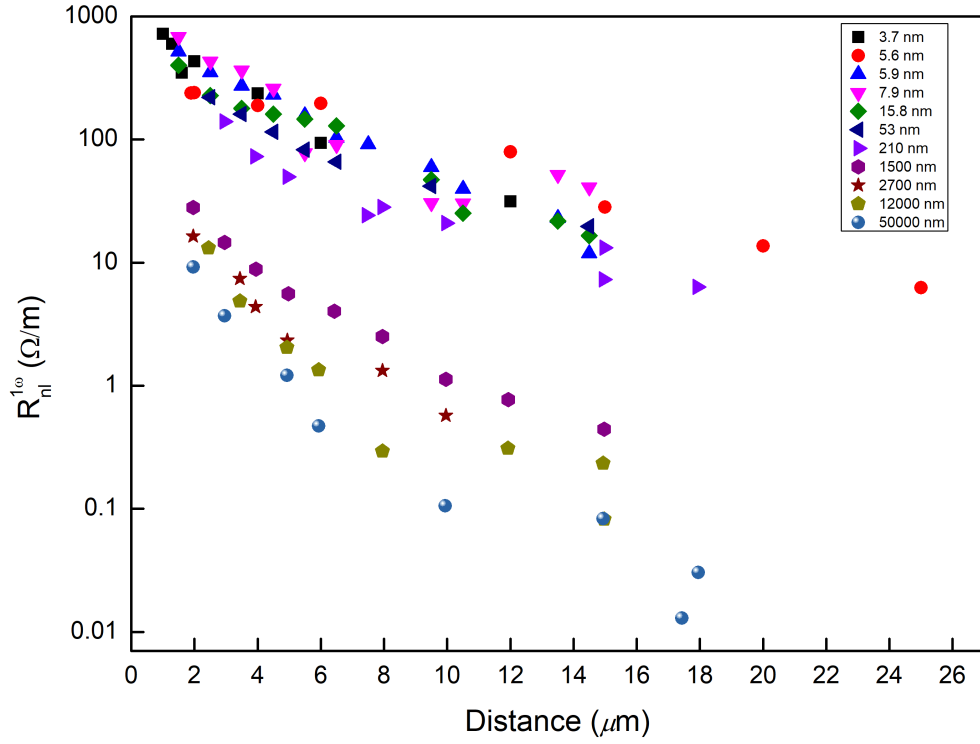


Figure 3: Non-local resistance as a function of injector-detector distance of the samples of series A and t_{YIG} varying from 3.7 nm to 50000 nm. The width of injector/detector is 400 nm. The results for $t_{\text{YIG}} \geq 210$ nm are adopted from Cornelissen et al.⁶ and Shan et al.²².

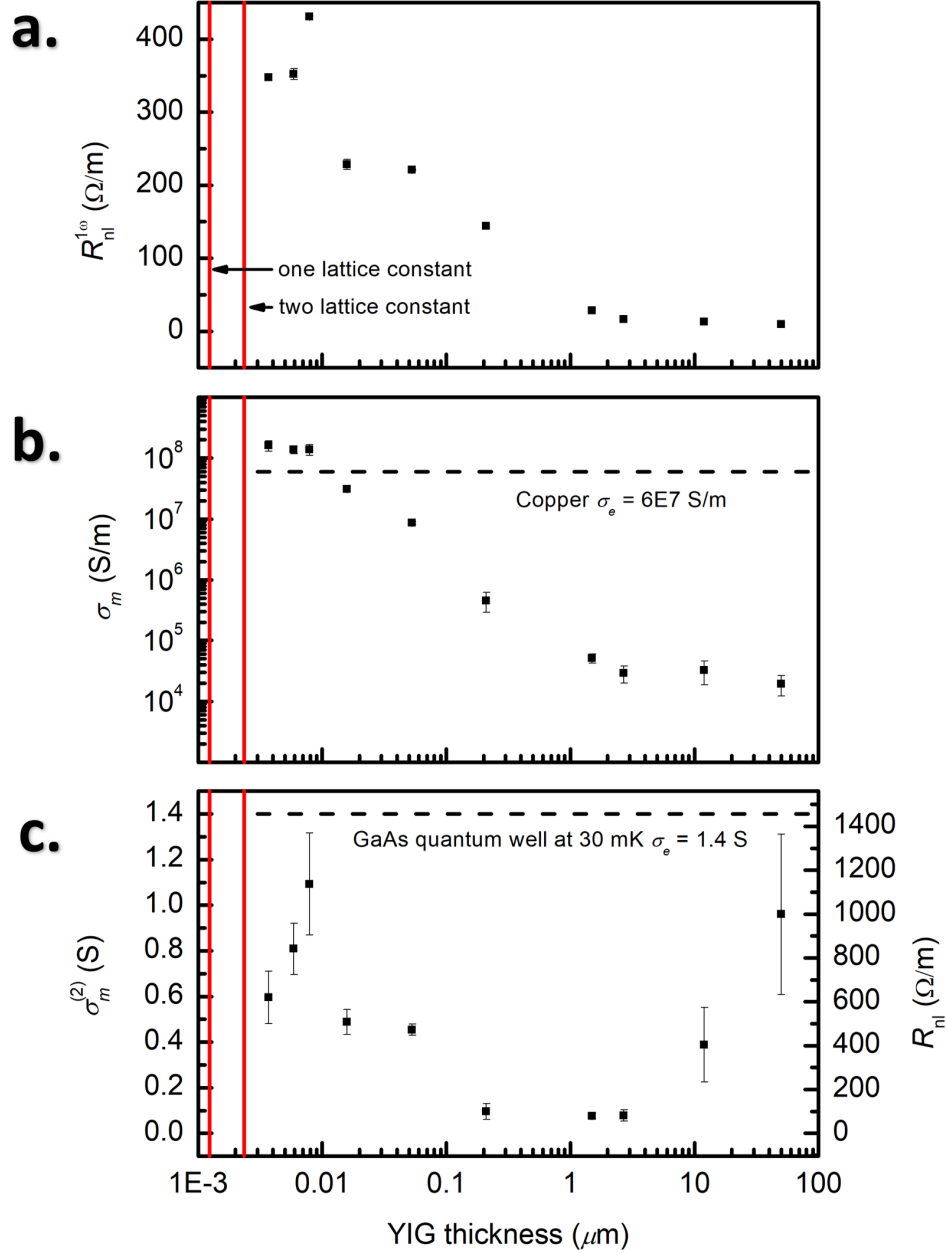


Figure 4: **a)** The non-local resistance $R_{\text{nl}}^{1\omega}$ at $d = 2.5 \mu\text{m}$ as a function of t_{YIG} . The results for $t_{\text{YIG}} \geq 210 \text{ nm}$ are adopted from Cornelissen et al.⁶ and Shan et al.²². **b)** Thickness dependence of the magnon conductivity σ_m obtained by the best fit for different distances with statistical error bars. **c)** Thickness dependence of the 2-dimension spin conductance $\sigma_m^{(2)}$ and the non-local resistance R_{nl} from the simulation, values based on the best fit for the magnon conductivity. The saturation at $t_{\text{YIG}} \rightarrow 0$ indicates that the film approaches the two-dimensional regime in ultrathin limit. The obtained error bar here means the range of the best fitting results for the non-local resistance we can get from the FEM simulations (see SI Section II).

Giant magnon spin conductivity approaching the two-dimensional transport regime in ultrathin yttrium iron garnet films

X-Y. Wei, O. Alves Santos, C.H. Sumba Lusero, G. E. W. Bauer, J. Ben Youssef, and B. J. van Wees

I. FINITE-ELEMENT MODELLING

We measure magnon transport non-locally by monitoring the voltage in a Pt detector as a function of current a Pt injector. The electrical spin accumulation μ_s (expressed in energy), which is generated by a current I in the injector at the YIG interface reads [S1]

$$\mu_s = 2eI\theta_{\text{Pt}} \frac{l_s}{\sigma_e t w} \tanh \frac{t}{2l_s}, \quad (\text{S1})$$

where e , t , w , θ_{Pt} , l_s and σ_s are the electronic charge, the Pt film thickness, width, spin Hall angle, spin relaxation length, and conductivity of the Pt contact. With parameters in Table I the charge current to spin accumulation conversion coefficient $\eta_{\text{inj}} = \mu_s/(eI) = 0.05 \Omega$ when $w = 400 \text{ nm}$ and 0.21Ω when $w = 100 \text{ nm}$.

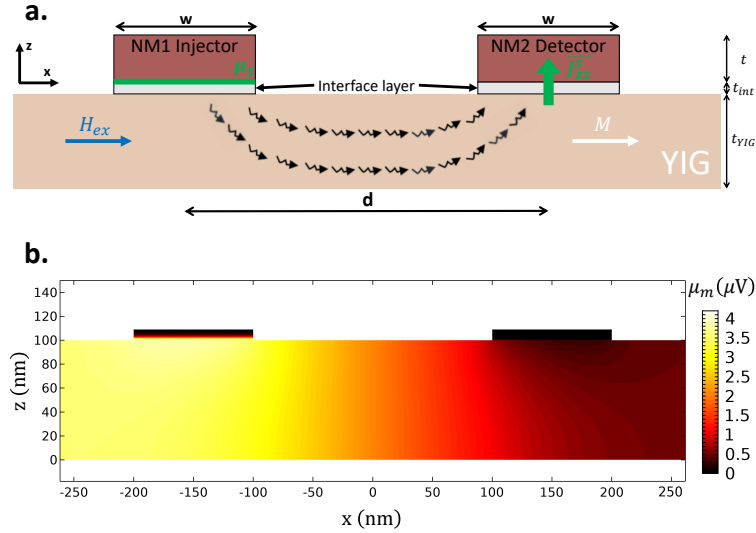


FIG. S1. **a)** The sample configuration and its dimensions in the model simulations. Eq. S1 and Eq. S4 describe the spin accumulation μ_s at the interface, used as input of the model, and the voltage build up in the detector, respectively. **b)** The magnon chemical potential profile for a 100 nm thick YIG film with a charge current $I = 20 \mu\text{A}$ and 100 nm wide injector/detector contacts and parameters in Table. I. Magnon absorption by the detector electrode causes the dark region close to the detector.

We calculate the diffusive magnon spin transport in YIG films numerically by finite-element method (FEM) [S2] in the configuration of Figure I a) using the COMSOL MULTIPHYSICS (version 5.4) software package. Since the length of the strips is much longer than the electrode separation, we use a 2D model, where the parameters depend on x and z only.

Ohm's Law for magnon current density \mathbf{j}_m in YIG is

$$\mathbf{j}_m = -\sigma_m \nabla \mu_m / e. \quad (\text{S2})$$

where $\nabla = \hat{x}\partial_x + \hat{z}\partial_z$ and σ_m is the magnon spin conductivity. The local magnon current is proportional to $\nabla \mu_m$. The diffusion equation

$$\nabla^2 \mu_m = \frac{\mu_m}{l_m^2}, \quad (\text{S3})$$

governs the magnon chemical potential μ_m , where l_m is the magnon relaxation length. We use the zero-current boundary condition $(\nabla \cdot \mathbf{n}) \mu_m = 0$ for the bottom as well as top surface that is not covered by Pt, where \mathbf{n} is the surface normal.

TABLE I. Parameters used to obtain the results in Figure I b) and Figure S2 b) and c).

Parameter	Symbol	Value
Magnon spin conductivity	σ_m	5×10^5 S/m (for 210 nm thickness YIG [S2])
Magnon spin relaxation length	l_m	5×10^{-6} m
Effective spin mixing conductance	G_s^{eff}	2×10^{12} S/m ²
Pt spin Hall angle	θ_{Pt}	0.11
Pt conductivity	σ_e	2×10^6 S/m
Pt spin relaxation length	l_s	1.5×10^{-9} m

The spin accumulation in the detector generates an magnon transport driving force proportional to $\partial\mu_s/\partial z$ that leads to a measurable voltage by the integral over the cross-section $A = wt$

$$V_{nl} = \frac{\theta_{Pt}}{2A} \int_A \frac{\partial\mu_s}{\partial z} dA. \quad (S4)$$

The non-local resistance $R_{nl} = V_{nl}/(IL)$ (in unit of Ω/m) can be compared with the experimental results. The detector efficiency is the same as that of the injector, $\eta_{det} = \eta_{inj}$.

The conversion of spin accumulation in Pt into magnons in YIG is governed by an effective spin conductance G_s^{eff} , which is a certain fraction, ≈ 0.06 , of the spin mixing conductance [S3, S4]. It can be modelled by a hypothetical spacer between Pt and YIG with conductivity $\sigma_s^{int} = G_s^{eff} t_{int}$, where $t_{int} = 1$ nm is the spacer layer thickness.

Figure I b) shows the magnon chemical potential profile μ_m in a 100 nm thick YIG under a charge current of $I = 20 \mu A$. Injector and detector with $w = 100$ nm/ $t = 8$ nm have a center-to-center distance of 300 nm. Table I lists the parameters used to produce Figure Ib). The Pt detector strip acts as a spin sink, absorbing magnons and producing a dark YIG region at the bottom of the detector in Fig. Ib).

II. YIG FILM THICKNESS DEPENDENCE

We measured the non-local resistance in many samples in order to obtain the YIG film thickness and contact-distance dependence. Figure S2 a) shows the experimental results for the non-local resistance for 400 nm wide injector/detector, with center to center distance $d = 2.5 \mu m$, and for different YIG thicknesses t_{YIG} . We distinguish two regimes: when $t_{YIG} > l_m$, $R_{nl}^{1\omega}$ saturates at a small value that does not depend on t_{YIG} anymore. On the other hand, $R_{nl}^{1\omega}$ increases with decreasing YIG thickness when $t_{YIG} < l_m$, where l_m is the magnon relaxation length.

Figure S2 b) shows that the non-local resistance calculated with a constant magnon spin conductivity *decreases* when the YIG film become *thinner*. Figure S2 c) shows the results for selected d as a function of t_{YIG} that in contrast to experiments, show a completely different thickness dependence.

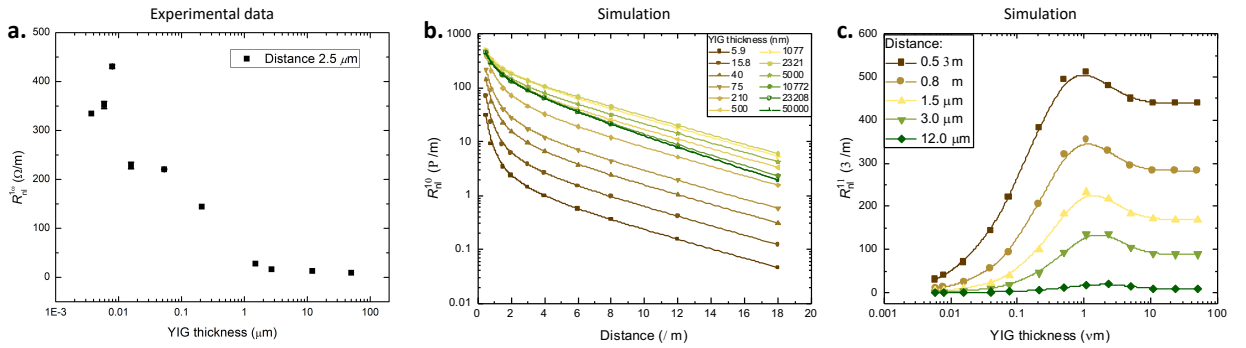


FIG. S2. **a)** YIG thickness dependence of the measured non-local signal $R_{nl}^{1\omega}$ for an injector/detector distance of $d = 2.5 \mu m$. **b)** Finite element model results with fixed magnon conductivity $\sigma_m = 5 \times 10^5$ S/m obtained previously for $t_{YIG} = 210$ nm [S2]. **c)** $R_{nl}^{1\omega}$ thickness dependency for different distances, for a fixed value of magnon spin conductivity. This shows an opposite trend in comparison with **a)**.

In Figure S2 c), $R_{nl}^{1\omega}$ saturates above $t_{YIG} > l_m$ because the magnon current distribution does not change anymore when increasing t_{YIG} . When $t_{YIG} < l_m$, on the other hand, the non-local resistance vanishes when $t_{YIG} = 0$, clearly is

opposite to the experimental trend. We have to conclude that σ_m dramatically increases the thin-film limit.

We now use σ_m as a single adjustable parameters that fits the experimental results. The numerical simulations are summarized in Figure S3 a) to j). The values of spin relaxation length used in the simulations, shown in Table II, were obtained from the experimental measurements at large distances, where the exponential decay is dominant[S5, S6].

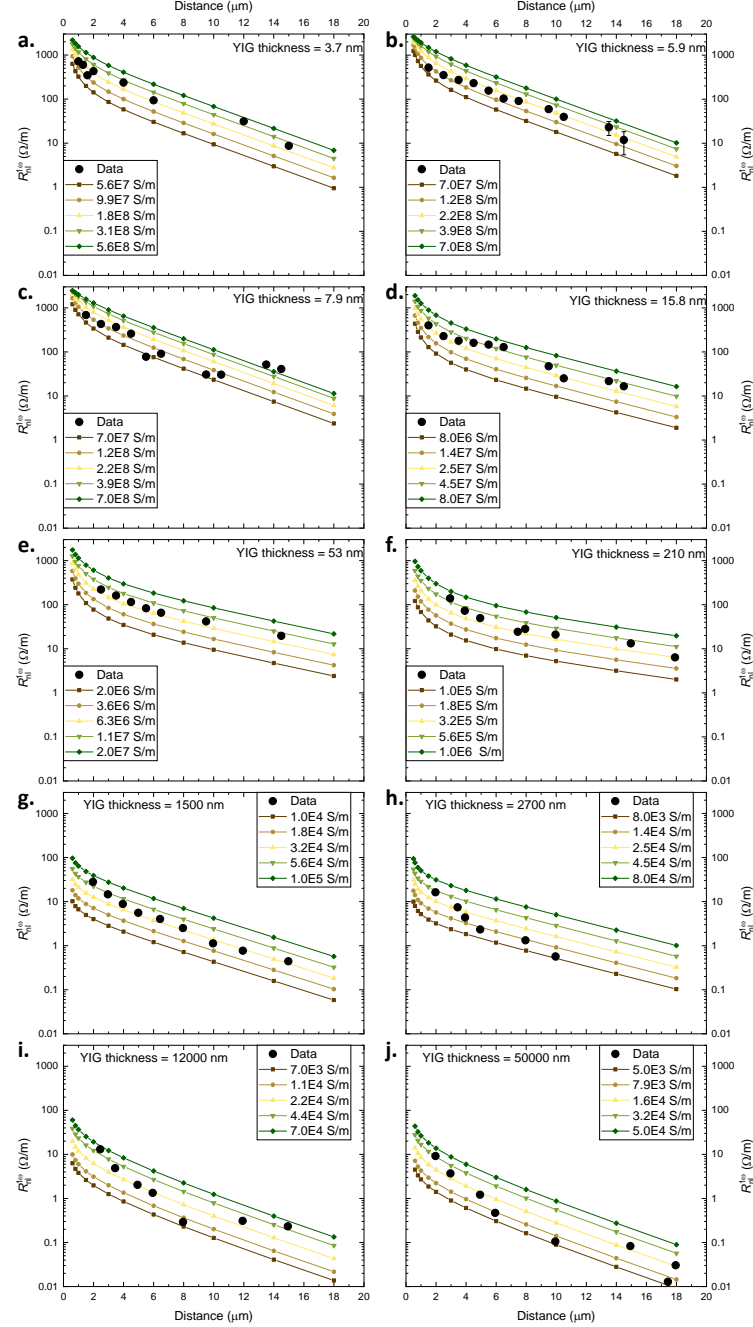


FIG. S3. Comparison between experimental data (black circles) and the two-dimensional diffusive model obtained for different values of the magnon spin conductivity σ_m , (lines brown to green). **a) to j)** present the distance dependence of the non-local resistance for different YIG thickness, from 3.7 nm up to 50 μm , indicated on the top of each figure. Based on that comparison we obtain the value of the magnon spin conductivity presented in Figure 5 of the main text.

Each black circle in Figure S3 is an independent measurement and susceptible to variations in the individual sample parameters. It is clear from Figure S3 that the experiments can be well fitted by a σ_m that depends on t_{YIG} .

TABLE II. Values of the magnon spin relaxation length adopted in the simulations.

YIG thickness [nm]	Spin relaxation length [μm]
5.9 / 7.9 / 15.8	3.5
53	6.0
210	9.2
1500	4.0
2700	3.5
12000 / 50000	4.0

III. PT|YIG INTERFACE SPIN RESISTANCE

The low interface magnon resistance resulting from the large effective spin mixing conductance makes the Pt strips act as a good spin source/sink. Figure S4 shows the calculated values of non-local resistance for wide range of effective spin conductance, G_s^{eff} . A significant change in the non-local resistance occurs only when we suppress G_s^{eff} to below $2 \times 10^{12} \text{ S/m}^2$. This value is lower than reported by Kohno et. al., $8.8 \times 10^{12} \text{ S/m}^2$ [S7] (after local annealing). In Figure S4, a higher G_s^{eff} does not significantly change the calculated non-local resistance, which represents that the giant increase of the non-local resistance we observed is not due to the increase of G_s^{eff} . Figure S5 shows an equivalent circuit model omitting magnon relaxation. The spin current passing through the circuit is dominated by the spin conductance of YIG since $R_{\text{int}}^s < R_{\text{YIG}}^s$. Therefore, R_{int}^s can be disregarded and the magnon transport measured by R_{nl} is determined by the magnon spin conductivity of YIG rather than the YIG|Pt interface conductance.

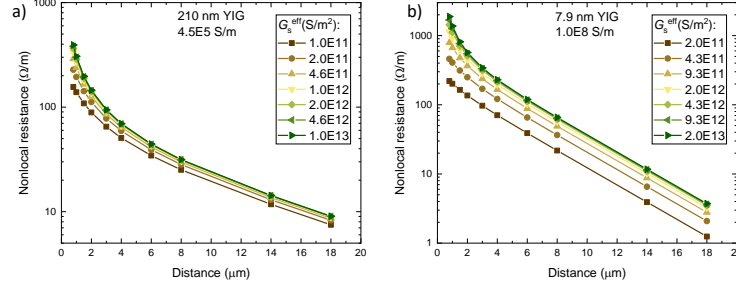


FIG. S4. Calculated non-local resistance for a range of values of the effective spin conductance G_s^{eff} of a 400 nm wide injector/detector. **a)** $t_{\text{YIG}} = 210 \text{ nm}$, and **b)** $t_{\text{YIG}} = 7.9 \text{ nm}$ YIG. In both cases, a significant change in the magnon transport only occurs for $G_s^{\text{eff}} < 2 \times 10^{12} \text{ S/m}^2$.

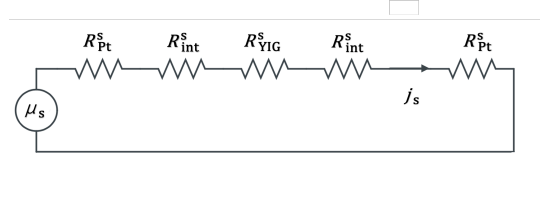


FIG. S5. This equivalent circuit model includes the relevant electronic and magnonic spin resistances and it is valid for short distance (within the magnon relaxation length). μ_s is the spin accumulation induced by the spin Hall effect. R_{Pt}^s is the spin resistance of the Pt strip (injector/detector). R_{int}^s is the interface spin resistance of Pt|YIG. j_s is the electronic spin current injected into the detector, and R_{YIG}^s is the spin resistance of YIG, which is the parameter of interest obtained from the two-dimensional model.

In an additional experiments we placed a third Pt strip between the injector and detector contacts. By absorbing magnons, the middle strip suppresses the non-local signal by a factor of 5 when $d = 2 \mu\text{m}$ and $t_{\text{YIG}} = 7.9 \text{ nm}$, and by a factor of 2 for $d = 4 \mu\text{m}$ and $t_{\text{YIG}} = 53 \text{ nm}$. From this, we obtain a best fit with $G_s^{\text{eff}} \approx 2.5 \times 10^{12} \text{ S/m}^2$ for $t_{\text{YIG}} = 7.9 \text{ nm}$,

and $G_s^{\text{eff}} \approx 1.0 \times 10^{12} \text{ S/m}^2$ for $t_{\text{YIG}} = 53 \text{ nm}$. We therefore adopted $G_s^{\text{eff}} = 2 \times 10^{12} \text{ S/m}^2$ as the standard value for the effective spin conductance in the other simulations.

We confirm the high G_s^{eff} by comparing results for different widths of the injector/detector contacts. The non-local resistance from the Series B devices in Figure S6 with width $w = 100 \text{ nm}$, is roughly 10 times higher than that of Series A devices with $w = 400 \text{ nm}$, which is mainly due to the higher values of the injector/detector conversion efficiency, Eq. S1. The simulations show that when G_s^{eff} is large, magnons are injected/absorbed predominantly in/by only part of the interfaces, i.e., the magnon chemical potential in the YIG film covered by the Pt strip decays according to an absorption length $L_{\text{absorb}} = \sqrt{\sigma_m t_{\text{YIG}} / G_s^{\text{eff}}}$ as sketched in Figure S7 b) in terms of the interface chemical potential μ_m and spin current, \vec{J}_s , in the Pt detector. Figure S7 a) shows the calculated resistance for $G_s^{\text{eff}} = 2 \times 10^{12} \text{ S/m}^2$, $\sigma_m = 1 \times 10^8 \text{ S/m}$, $t_{\text{YIG}} = 3.7 \text{ nm}$ and therefore $L_{\text{absorb}} = 430 \text{ nm}$ that agrees with observations. This confirms our value for G_s^{eff} even for the thinnest films.

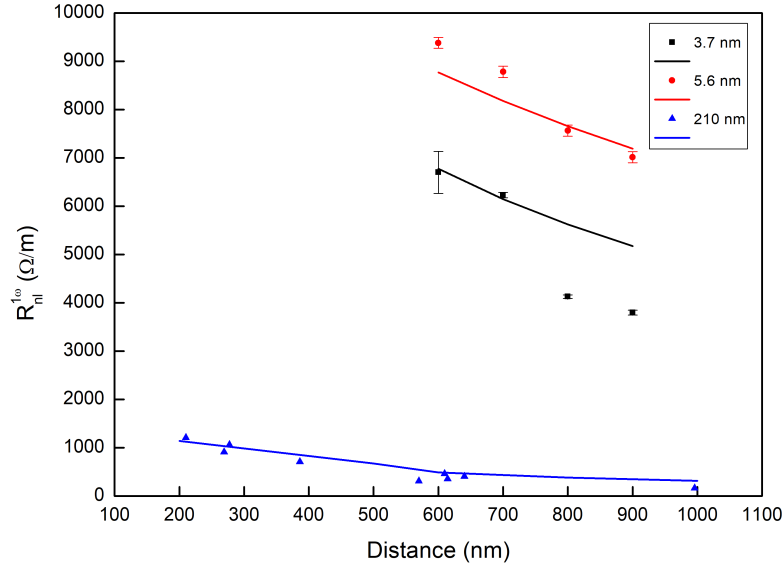


FIG. S6. Non-local resistance as a function of injector-detector separation distance for series B devices. The thickness of YIG films is 3.7 nm and 210 nm. The non-local resistance of 3.7 nm thickness YIG is more than ten times larger than that in 210 nm thickness YIG at same center-to-center distance. The lines are the simulation results based on a 2D-FEM model. The magnon conductivities σ_m here are $1.0 \times 10^8 \text{ S/m}$ for 3.7 nm, $1.45 \times 10^8 \text{ S/m}$ for 5.6 nm and $4.5 \times 10^5 \text{ S/m}$ for 210 nm thickness YIG.

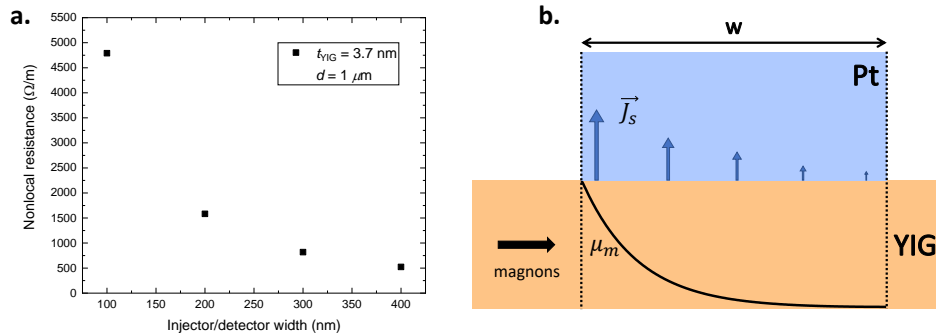


FIG. S7. **a)** Simulation for the non-local resistance with different injector/detector width on 3.7 nm thickness YIG. The center-to-center distance between the injector and the detector is $1 \mu\text{m}$. The simulations in Figure S7 are in agreement with the experimental results in Figure S6. **b)** Schematic illustration of the decay of the magnon chemical potential decay and spin current over the Pt width.

IV. MAGNETIC PROPERTIES OF THE YIG FILMS

Table. III summarizes the magnetic properties of the YIG films are determined by broadband ferromagnetic resonance in the range of 2-40 GHz. The magnon spin relaxation lengths obtained by fitting Eq. 3 in the main text, are shown in Figure. S8.

TABLE III. Magnetic properties of the YIG films by FMR characterization.

YIG thickness t_{YIG} (nm)	Gilbert damping α (10^{-4})	Effective field $H_{\text{eff}} = H_k - 4\pi M_s$ (Oe)	Inhomogenous linewidth ΔH_{inh} (Oe)
3.7	5 ± 2.1	1720	17
5.6	not available	1900	not available
5.9	10 ± 2.4	1950	43
7.9	6.3 ± 4.6	1930	53
15.8	0.6 ± 0.5	1960	7.9
53	1.0 ± 0.2	1810	1

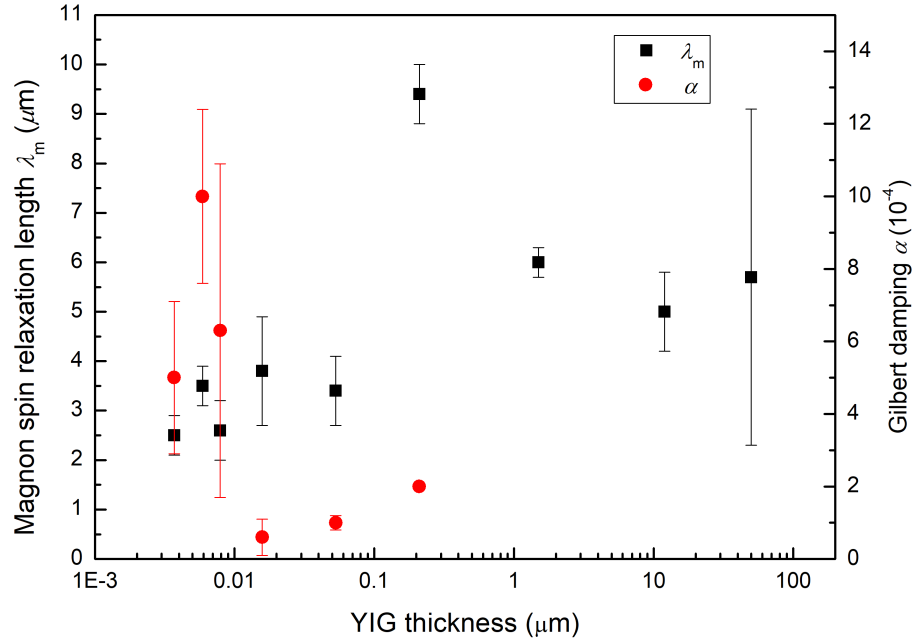


FIG. S8. Magnon spin relaxation length and Gilbert damping parameter as a function of YIG film thickness. The thickness of YIG films ranges from 3.7 nm to 50000 nm (shown on a logarithmic scale). The results from 210 nm to 50000 nm thickness samples are adopted from Cornelissen et al.[S5] and Shan et al.[S6]. The Gilbert damping parameter of the YIG films is also presented here. Note that for ultrathin YIG (around 10 nm), the magnon spin relaxation lengths are similar to each other but the Gilbert damping parameters are quite different.

V. THE SECOND HARMONIC NON-LOCAL RESISTANCE

The second harmonic signal in the non-local resistance is a measure of the thermal spin generation in the magnetic film by the spin Seebeck effect. Figures. S9 a) shows results for this $R_{\text{nl}}^{2\omega}(\alpha)$ as a function of the direction of in-plane magnetic field. $R_{\text{nl}}^{2\omega}$ can be extracted by

$$R_{\text{nl}}^{2\omega}(\alpha) = 1/2 R_{\text{nl}}^{2\omega} \cos \alpha + R_0^{2\omega}, \quad (\text{S5})$$

where α is the in-plane angle of \mathbf{H}_{ex} with the x -axis. $R_0^{2\omega}$ is an offset signal, possibly by an unintended conventional Seebeck voltage in the detector[S8]. We plot the observed amplitude $R_{\text{nl}}^{2\omega}$ as a function of contact separation in Figures. S9 b) for $t_{\text{YIG}} = 5.9$ nm, 7.9 nm, 15.9 nm (series A with 400 nm wide injector/detector strips). $R_{\text{nl}}^{2\omega}$ in ultrathin YIG is significantly reduced compared to that in thicker YIG films[S5, S6, S9], because the generation of thermal magnons by SSE due to the vertical temperature gradient become less effective. Figures. S9 b) show neither a simple Ohmic or exponential decay as a function of d , which indicates that the generation and transport of magnons is complex and requires detailed modelling of the temperature profile. Just like the magnon conductivity, the spin Seebeck coefficient should also depend on t_{YIG} . A reliable extraction of both parameters as a function of thickness from the second harmonic signals appears impossible at this time.

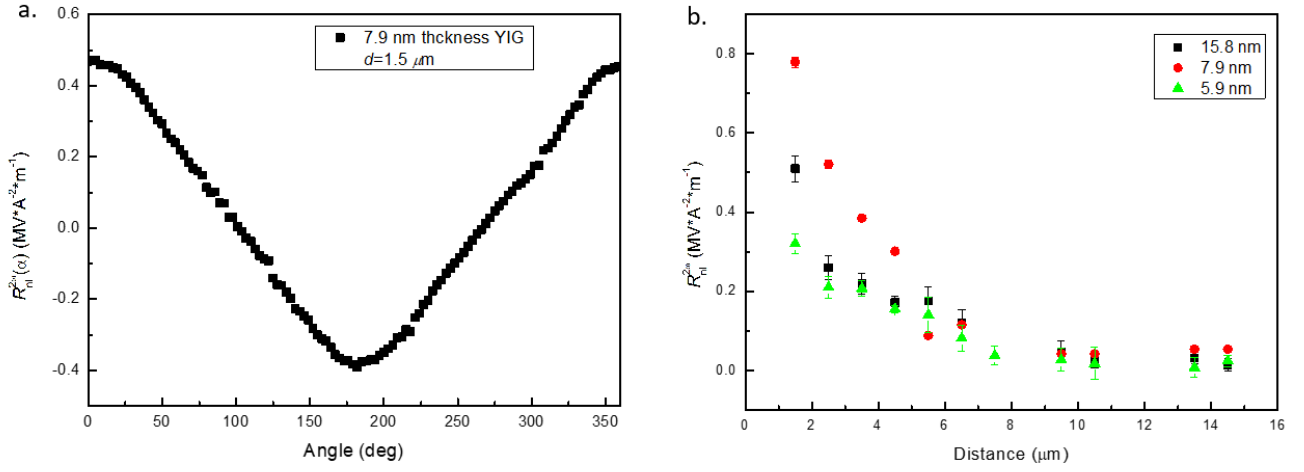


FIG. S9. The second harmonic non-local signals of ultrathin YIG films. **a)** The angle-dependence for $t_{\text{YIG}} = 7.9$ nm and center-to-center distance of injector and detector $d = 1.5 \mu\text{m}$. **b)** Amplitude of the non-local signals as a function of d for the samples from series A.

VI. MAGNETIC FIELD DEPENDENCE OF THE NON-LOCAL SIGNAL IN ULTRATHIN FILMS

We measured the non-local transport in the series A devices with $t_{\text{YIG}} = 5.9$ nm (Figure. S10) and $t_{\text{YIG}} = 7.9$ nm (Figure. S11) as a function of the strength of a magnetic field along x (in-plane, normal to the contacts). We use Eq. 3 from the main text to extract the field-dependence of the magnon conductivity and relaxation length, as shown in Figure. S12 and Figure. S13, where we use $\eta_{\text{cs}} = \eta_{\text{sc}} = 0.05 \Omega$ from Section I.

While the magnon spin relaxation length only slightly decreases, the increasing field suppresses the magnon spin conductivity stronger for the thinner samples. This is in line with the dominance of the lowest magnon subband in the thinnest samples, which is more susceptible to magnetic freeze-out of the thermal magnon population.

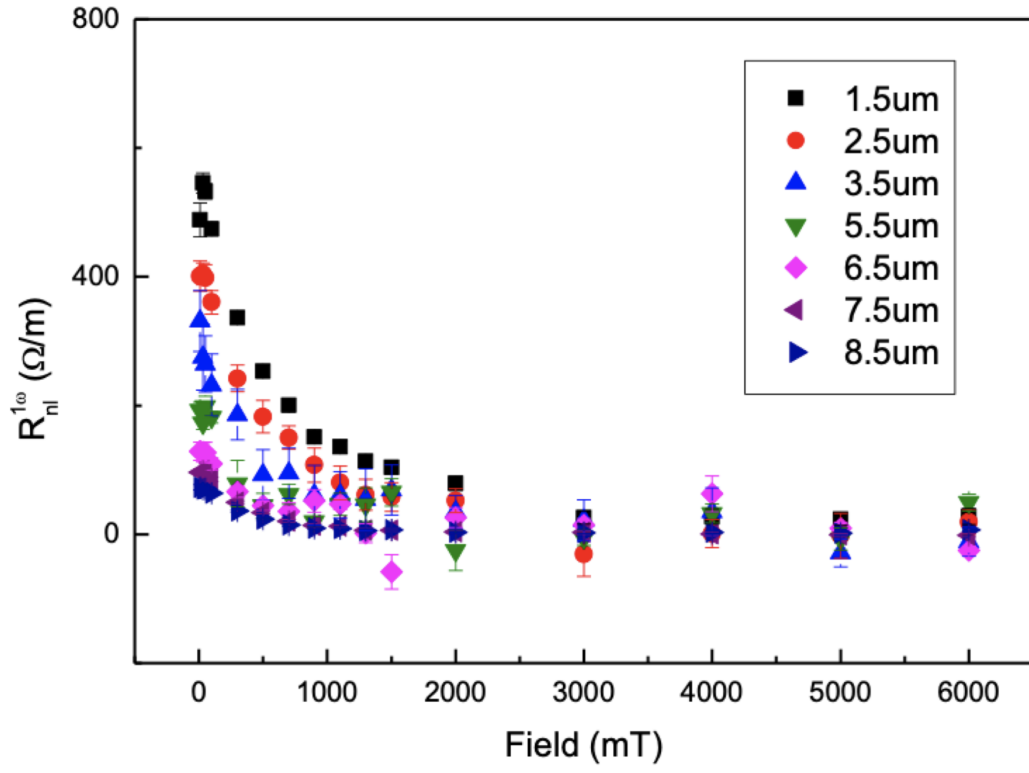


FIG. S10. The non-local resistance $R_{nl}^{1\omega}$ as a function of magnetic field and contact distance of the A series sample with $t_{YIG} = 5.9$ nm.

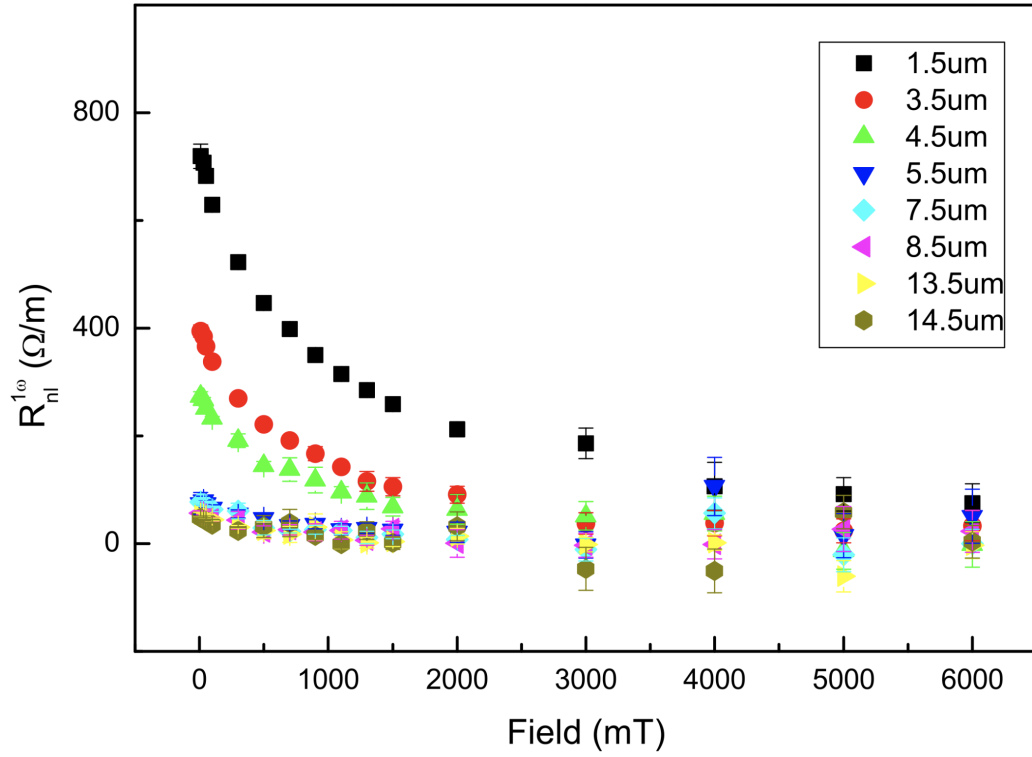


FIG. S11. The non-local resistance as function of magnetic field for $t_{YIG} = 7.9$ nm.

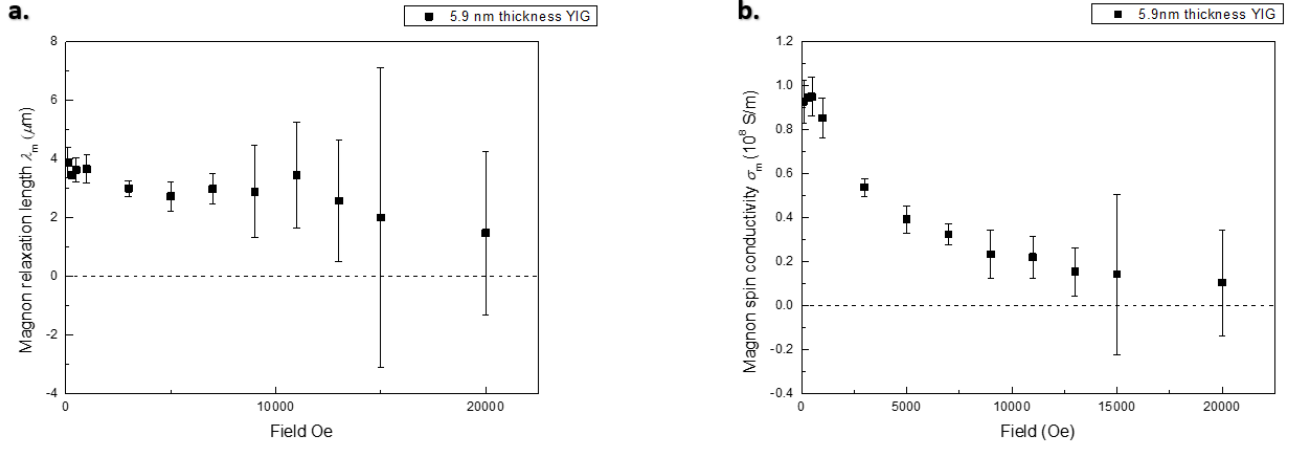


FIG. S12. λ_m and σ_m as a function of field in a film with $t_{\text{YIG}} = 5.9$ nm. **a)** The magnon relaxation length λ_m decreases slightly with increasing magnetic field. **b)** The magnetic field strongly suppresses the magnon conductivity σ_m .

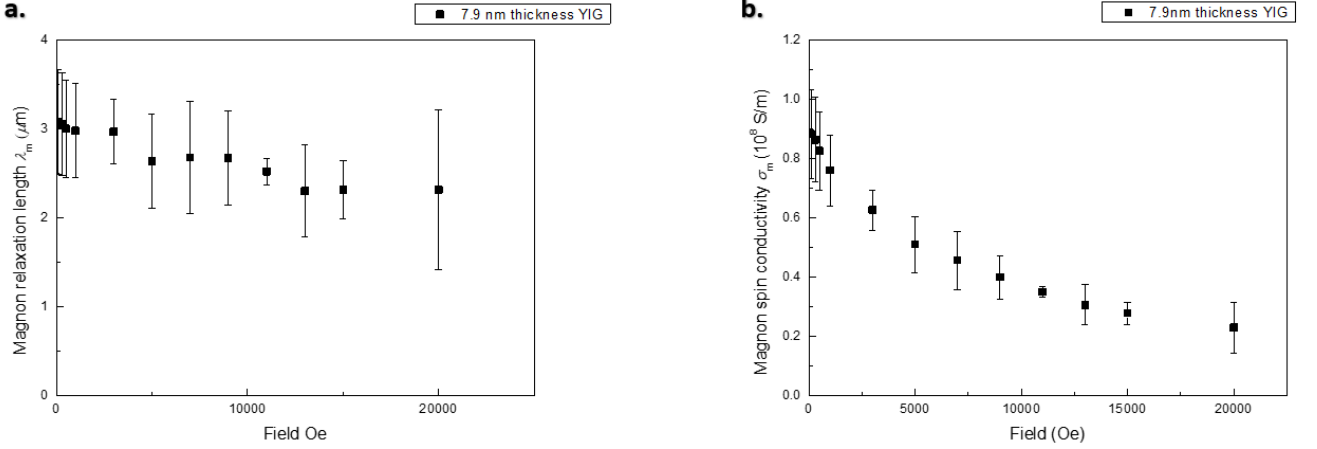


FIG. S13. **a)** λ_m and **b)** σ_m , as a function of field in a film with $t_{\text{YIG}} = 7.9$ nm.

VII. TEMPERATURE DEPENDENCE OF THE NON-LOCAL SIGNAL IN ULTRATHIN FILMS

We measured the temperature dependence of the non-local signal on series A samples with $t_{\text{YIG}} = 3.7$ nm (Figure. S14), 5.9 nm (Figure. S15) and 7.9 nm (Figure. S16) and a magnetic field of 50 mT. $R_{\text{nl}}^{1\omega}$ for $t_{\text{YIG}} = 3.7$ nm at low temperatures is more than five times larger for $d = 1.3 \mu\text{m}$ than for $d = 2 \mu\text{m}$. Since the decrease of G_s^{eff} due to the temperature is equivalent for both devices. The large change of the ratio of $R_{\text{nl}}^{1\omega}$ for $d = 1.3 \mu\text{m}$ and $d = 2 \mu\text{m}$ suggests that $R_{\text{nl}}^{1\omega}$ is dominated by the magnon spin conductivity of YIG and not the Pt|YIG interface spin conductance, which supports the conclusions from Section III.

Results of the fit by Eq. 3 from the main text are shown in Figure. S17 and Figure. S18. The magnon relaxation length only slightly changes with temperature, in contrast to that σ_m decreases strongly with temperature. In thick YIG films, $R_{\text{nl}}(T)$ decreases slowly at high temperatures and faster at low temperatures [S10, S11], but the decrease at low temperatures is much more pronounced for ultrathin thickness YIG. Also this result is consistent with the dominant role of the lowest magnon subband in thermal transport in the thinnest films, since the two-dimensional magnon gas is more susceptible to the freeze out of carriers at low temperatures.

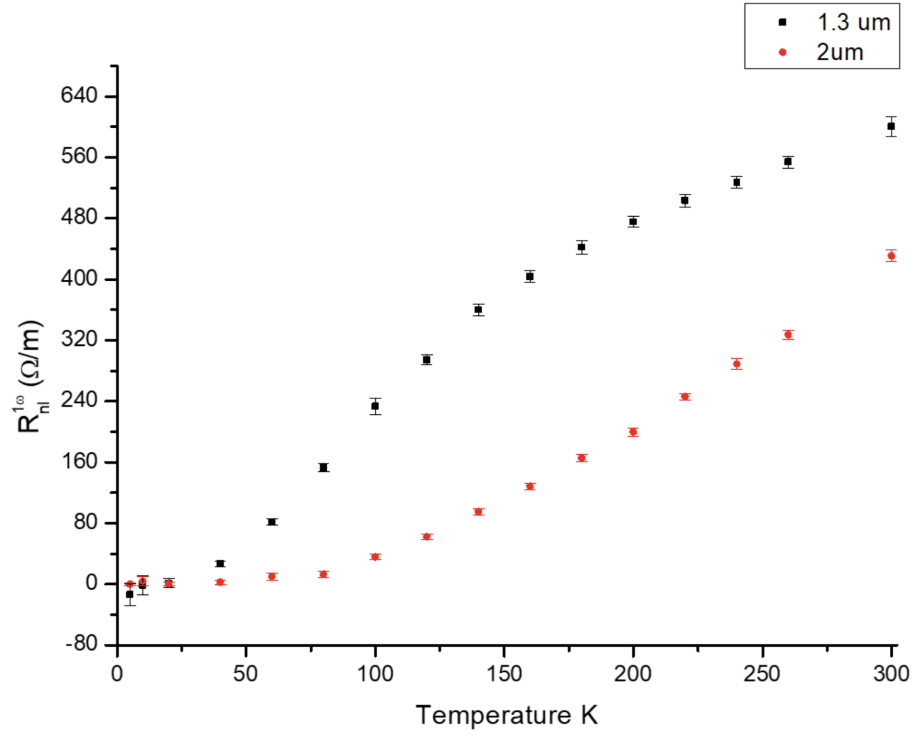


FIG. S14. The non-local resistance $R_{nl}^{1\omega}$ as a function of temperature for different contact distances on a YIG film with $t_{YIG} = 3.7$ nm.

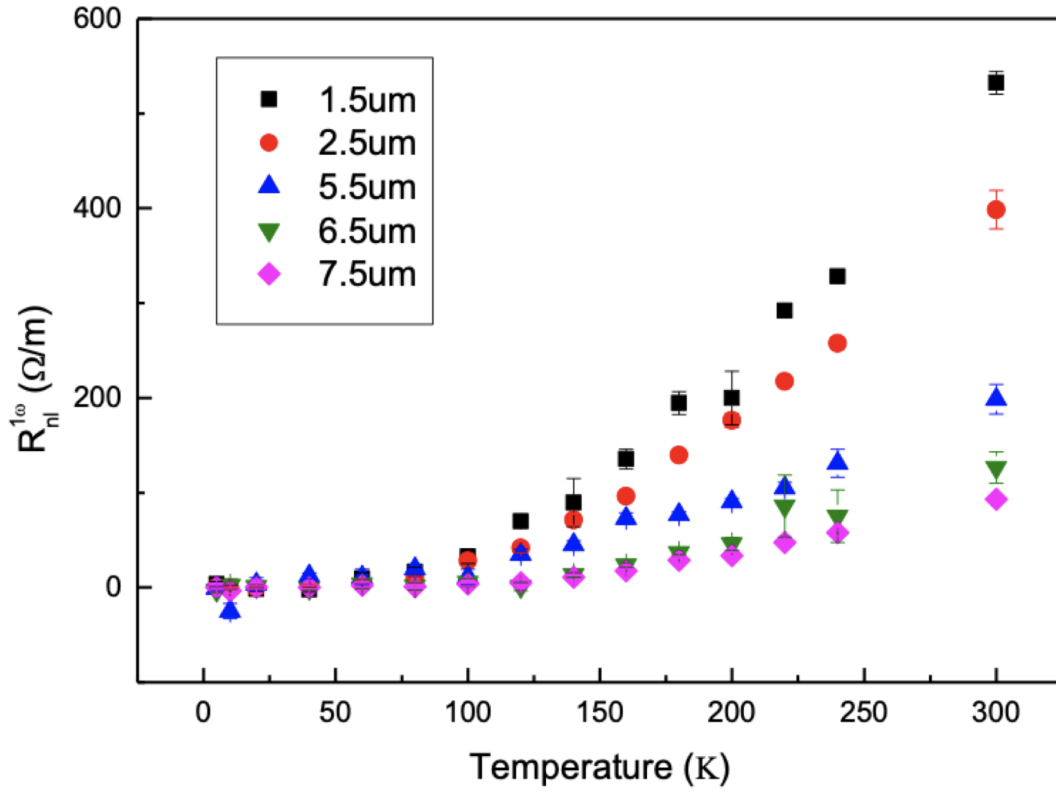


FIG. S15. Non-local resistance as a function of temperature for $t_{YIG} = 5.9$ nm.

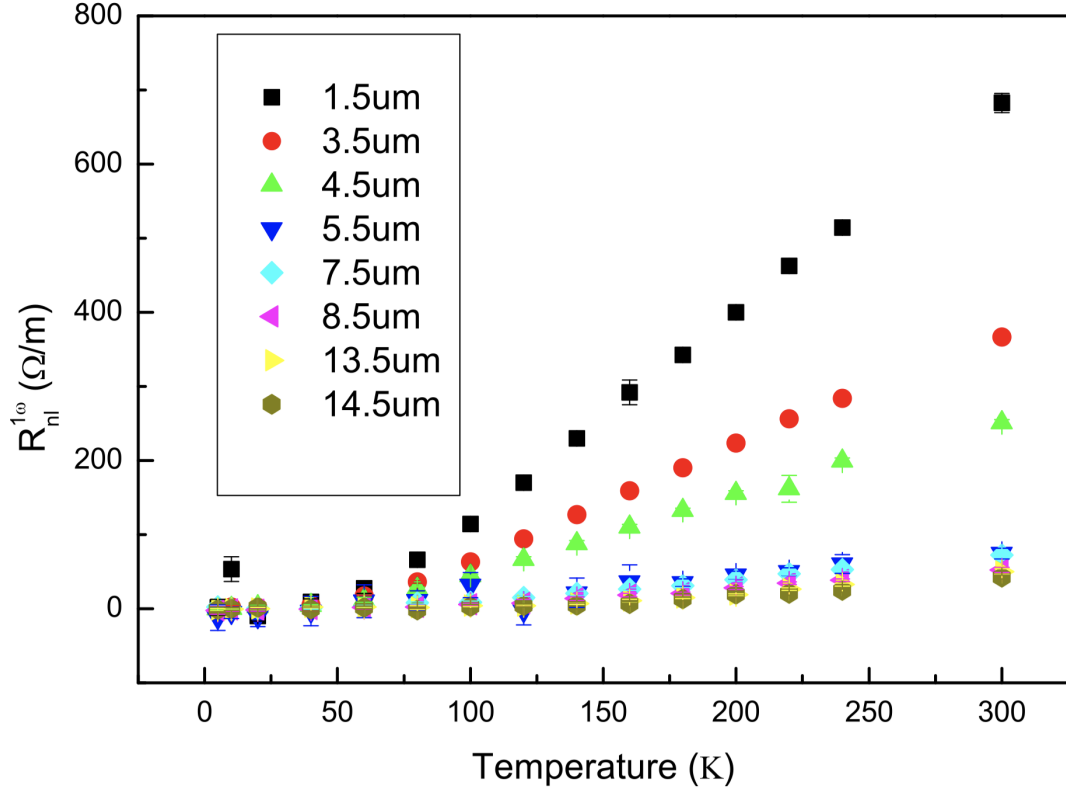


FIG. S16. Non-local resistance as a function of temperature for $t_{\text{YIG}} = 7.9$ nm.

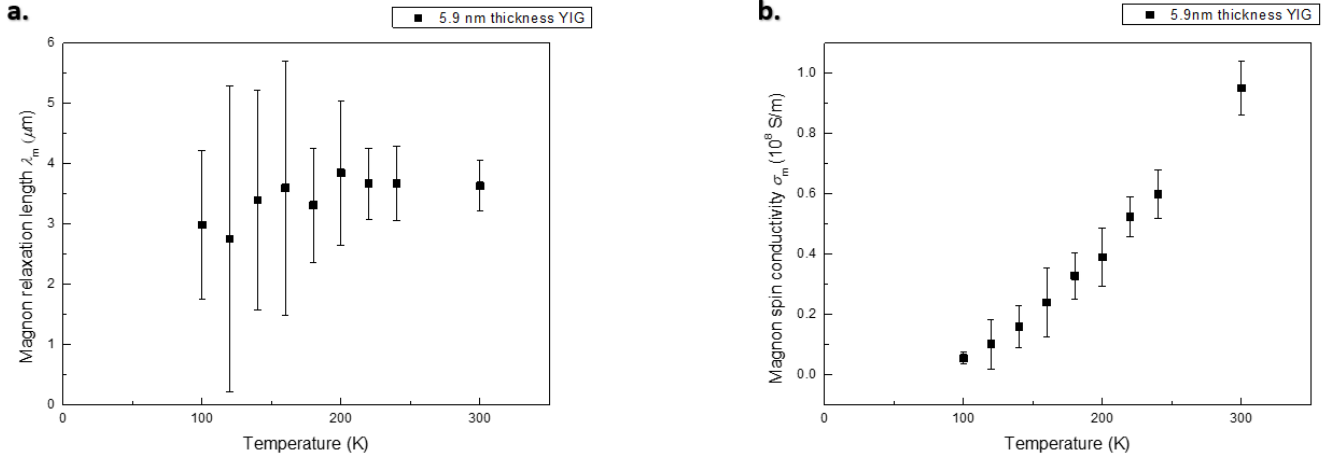


FIG. S17. **a)** λ_m and **b)** σ_m as a function of temperature for $t_{\text{YIG}} = 5.9$ nm.

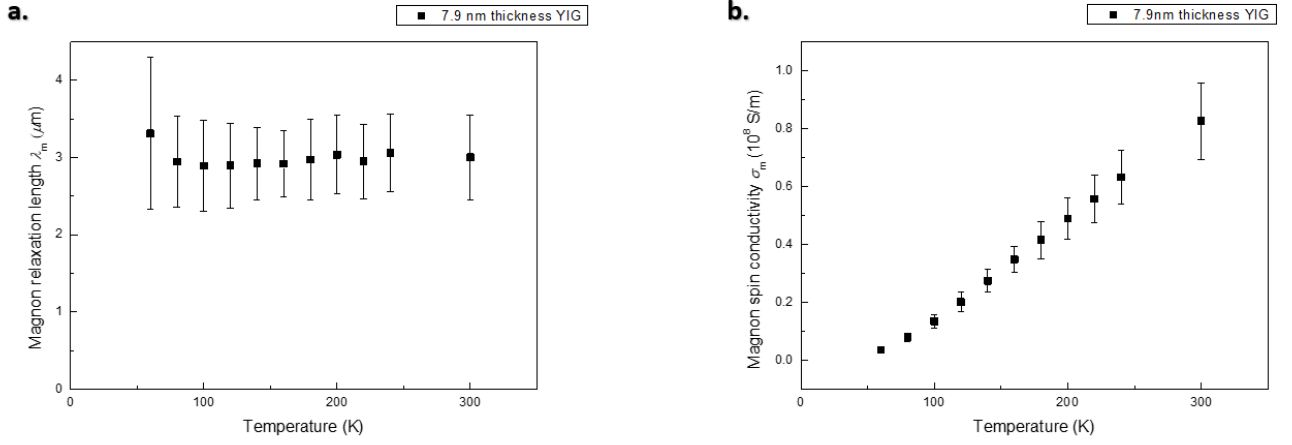


FIG. S18. **a)** λ_m and **b)** σ_m as a function of temperature for $t_{\text{YIG}} = 7.9$ nm.

VIII. HIGHEST OCCUPIED EXCHANGE MODE OF YIG AT ROOM TEMPERATURE

Figure. S19 shows the highest occupied exchange perpendicular standing spin waves (PSSW) 2D subbands n for different thickness YIG films at room temperature. The number of the occupied subbands is $n + 1$. It is reduced from over 10^4 to a few when the thickness of the films is down to 3.7 nm.

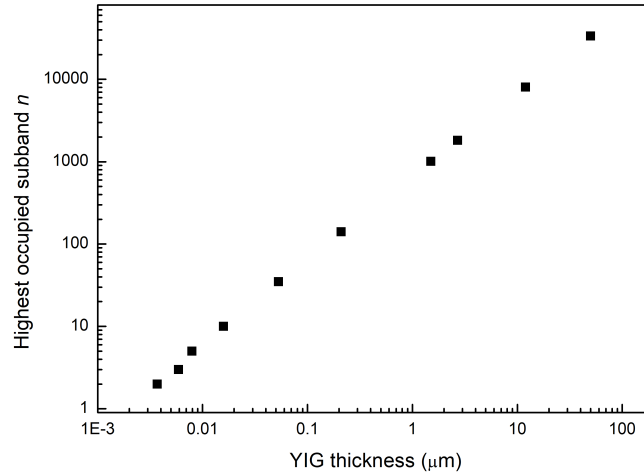


FIG. S19. Thickness dependency of the number of occupied PSSW modes defined as the highest occupied subband n at 300 K.

-
- [S1] Sinova, J., Valenzuela, S. O., Wunderlich, J., Back, C. H. & Jungwirth, T. Spin Hall effects. *Rev. Mod. Phys.* **87**, 1213–1260 (2015).
- [S2] Cornelissen, L. J., Peters, K. J. H., Bauer, G. E. W., Duine, R. A. & van Wees, B. J. Magnon spin transport driven by the magnon chemical potential in a magnetic insulator. *Phys. Rev. B* **94**, 014412 (2016).
- [S3] Weiler, M. *et al.* Experimental Test of the Spin Mixing Interface Conductivity Concept. *Phys. Rev. Lett.* **111**, 176601 (2013).

- [S4] Qiu, Z. *et al.* Spin mixing conductance at a well-controlled platinum/yttrium iron garnet interface. *Applied Physics Letters* **103**, 092404 (2013).
- [S5] Cornelissen, L. J., Liu, J., Duine, R. A., Ben Youssef, J. & van Wees, B. J. Long-distance transport of magnon spin information in a magnetic insulator at room temperature. *Nature Physics* **11**, 1022–1026 (2015).
- [S6] Shan, J. *et al.* Influence of yttrium iron garnet thickness and heater opacity on the nonlocal transport of electrically and thermally excited magnons. *Phys. Rev. B* **94**, 174437 (2016).
- [S7] Kohno, R. *et al.* Enhancement of YIG |Pt spin conductance by local Joule annealing. *Applied Physics Letters* **118**, 032404 (2021).
- [S8] Sierra, J. F. *et al.* Thermoelectric spin voltage in graphene. *Nature Nanotechnology* **13**, 107–111 (2018).
- [S9] Shan, J. *et al.* Criteria for accurate determination of the magnon relaxation length from the nonlocal spin Seebeck effect. *Phys. Rev. B* **96**, 184427 (2017).
- [S10] Cornelissen, L. J., Shan, J. & van Wees, B. J. Temperature dependence of the magnon spin diffusion length and magnon spin conductivity in the magnetic insulator yttrium iron garnet. *Phys. Rev. B* **94**, 180402 (2016).
- [S11] Gomez-Perez, J. M., Vélez, S., Hueso, L. E. & Casanova, F. Differences in the magnon diffusion length for electrically and thermally driven magnon currents in $\text{Y}_3\text{Fe}_5\text{O}_{12}$. *Phys. Rev. B* **101**, 184420 (2020).